Supporting Information for

Sodium Drives Interfacial Equilibria for Semi-Soluble Phosphoric and Phosphonic Acids of Model Sea Spray Aerosol Surfaces

Jennifer F. Neal[†], Mickey M. Rogers[†], Morgan A. Smeltzer, Kimberly A. Carter-Fenk, Alexander J. Grooms, Mia M. Zerkle, Heather C. Allen[*]

Department of Chemistry & Biochemistry, The Ohio State University, Columbus, OH 43210, United States

[†]These authors contributed equally to this work

*Corresponding author E-mail: allen@chemistry.ohio-state.edu

Table of Contents

1. MATERIALS AND METHODS

1.1 Materials

All materials were purchased in high purity and used without further purification. 1-palmitoyl-2-hydroxy-sn-glycero-3-phosphate sodium salt (>99%, Avanti Polar Lipids), 1,2-didecanoyl-sn-glycero-3-phosphate sodium salt (>99%, Avanti Polar Lipids), 1,2-dioctanoyl-sn-glycero-3-phosphate sodium salt (>99%, Avanti Polar Lipids), and 1-stearoyl-2-hydroxy-sn-glycero-3-phosphate sodium salt (>99%, Avanti Polar Lipids) were dissolved in a 65:35:8 chloroform/methanol/water (v/v/v) (HPLC grade, Fisher Scientific). Stock solutions of hexadecylphosphonic acid (97%, Sigma Aldrich) and octadecylphosphonic acid (97%, Sigma Aldrich) were dissolved in a mixture of 4:1 chloroform/methanol (v/v) and/or pure chloroform (HPLC grade, Fisher Scientific). Sodium chloride (ACS certified, Fisher) was baked at 650°C for 10 hours prior to use to remove organic impurities.[1] The pH adjusted solutions were made with hydrochloric acid (trace metal grade, Fisher Scientific) in ultrapure water with a resistivity of 18.2 MΩ·cm (Milli-Q Advantage A10). The pH values of all final solutions were recorded using a Thermo Scientific Orion Versa Star Pro (± 0.002 pH units). The pH of pure water and NaCl solutions (in equilibrium with atmospheric CO_2) were measured to be 5.6. For convenience, the bulk pH values adjusted with HCl will be referred to their nearest integer value within ± 0.25 pH units (1, 2, 3, 4). All experiments were performed at ambient temperature 22.3 ± 0.8 °C with a relative humidity of 38 % ± 10 %.

1.2 Surface pressure-area isotherms

The procedure for surface pressure–area isotherms has been previously described.[2] In brief, the semi-soluble species in the solvent solutions were spread dropwise onto the pH adjusted solutions in a Langmuir trough (Biolin Scientific USA, Paramus, NJ). After solvent evaporation, Delrin barriers compressed symmetrically at a rate of 5 mm/min/barrier and the surface pressure was measured using Wilhelmy filter paper plates (Ashless grade, Whatman). All isotherms were performed in at least triplet and processed using Origin software (OriginLab, Northampton, MA). The average function on Origin was used to average at least three isotherms and one standard deviation is shown on the plots as the shaded region.

1.3 Brewster angle microscopy

Brewster angle microscopy (BAM) was performed using a custom-built BAM microscope previously described.[3] In summary, *p*-polarized 543 nm light was reflected off the aqueous surface at the Brewster angle and collected by an Andor CCD camera. The final BAM images shown in the Supporting Information were cropped down from their full size (800 μm x 800 μm) to (480 μm x 480 μm) to display the most resolved region. A blue color scale with gray level range 1-100 was chosen to enhance image contrast. The images with light blue and white regions correspond to high lipid coverage while the dark blue regions correspond to low lipid coverage or the aqueous solution. The pure water and pH adjusted background images have gray levels <30.

1.4 Infrared reflection–absorption spectroscopy

Infrared reflection–absorption spectroscopy (IRRAS) spectra were recorded on an FT-IR spectrometer (Frontier, Perkin Elmer, United States) equipped with a liquid nitrogen cooled HgCdTe (MCT) detector. Petri dishes were placed inside the spectrometer on a breadboard that aligned two gold plated mirrors (50.8 mm) at an incident angle of 48° (relative to the surface

normal) to collect reflectivity off the monolayer and aqueous solutions. Spectra were plotted as reflectance–absorbance (RA) which is given as RA= -log(R_m/R_o). In this equation, R_m is the reflectivity of the monolayer and R_o is the reflectivity of the aqueous solution. Spectra were recorded as an average of 400 scans using unpolarized light in single beam mode. Data analysis was done using Origin software, and the spectra shown here are the average of at least three individual spectra. Each individual spectrum was offset prior to averaging in order to align the baselines of the spectra. Note that in the current geometry at an incidence angle of 48°, the peaks are observed as negative bands.

2. SUPPORTING RESULTS

2.1 Π-A isotherms for the C_{18} phosphonic acid and dioctanoyl PA

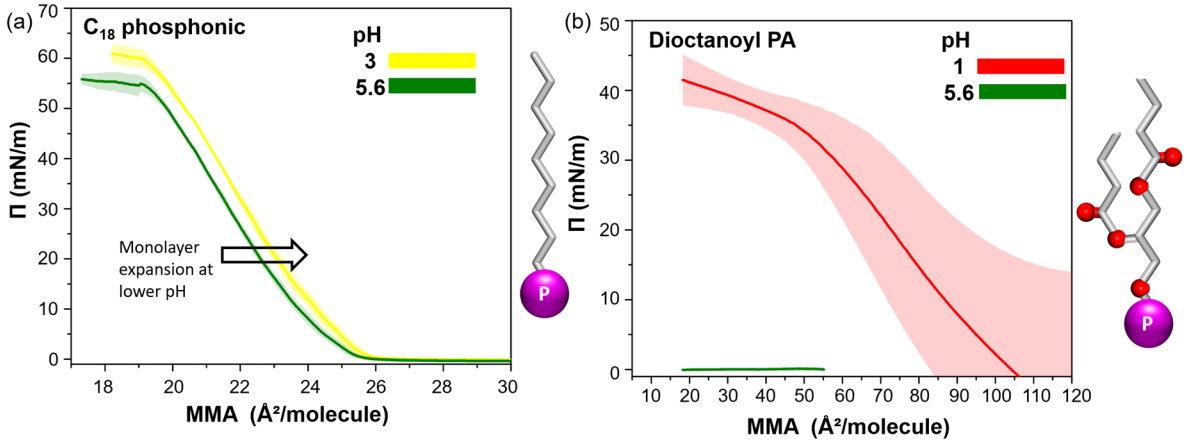

Figure S1. Π-A isotherms of the (a) C_{18} phosphonic acid on pH 3 and pH 5.6 and (b) dioctanoyl PA on pH 1 and pH 5.6.

Π-A isotherms of the C_{18} phosphonic acid and dioctanoyl PA are shown in Figure S1. Both molecules were not semi-soluble. C_{18} phosphonic acid is condensed at pH 5.6 compared to pH 3. The appearance of the deprotonated phosphonate species at higher pH could lead to an expansion in the monolayer due to both the size of the negative headgroup and electrostatic repulsion; however, the opposite is observed for this system. This agrees with previous studies of C_{18} phosphoric acid and partially protonated fatty acids, where they ascribe the contraction in the monolayer as a consequence of increasing headgroup interactions.[4–6] It is not surprising that the mixed protonation state monolayer shows this condensing effect in the isotherm since the charged species is a better hydrogen bonding acceptor than the neutral species. Π-A isotherms for the C_{18} phosphonic acid on water (pH 5.6) have been previously published by Ries and Cook, and Woodward, et al. Our results are in good agreement with Ries and Cook, but not with Woodward et al., and this disparity can be attributed to different experimental conditions including compression speed.[7,8] Thus, there is a difference in solubility for the singly deprotonated species between C_{16} to C_{18} phosphonic acid, and this was also reported for the C_{16} to C_{18} phosphoric acid derivatives.[9]

The isotherm for dioctanoyl PA did not show a rise in surface pressure at pH 5.6, and at pH 1 multiple trials of isotherms showed inconsistent liftoff points (Figure S1b). Although we can reasonably assume that the molecule is fully protonated at pH 1 (the pK_{a1} of phosphoric acid in water is ~2.2),[10] it remains semi-soluble at this low pH. Didecanoyl PA, on the other hand, forms monolayers at low pH, with a liftoff point that is approximately 98 Å^2/molecule at pH 1 (Figure 3). It is then clear that didecanoyl PA, which has longer acyl chains, is more insoluble than dioctanoyl PA at pH 1. The liftoff point for didecanoyl PA is much larger than what could reasonably be expected for a highly packed species. For reference, the highly condensed

monolayer of dihexadecanoyl PA (DPPA) has a liftoff point of approximately 47.5 $Å^2$/molecule,[2] and the liftoff point of didecanoyl PA is greater than twice that of dihexadecanoyl PA. This highlights the effect of acyl chain length in the molecular packing of the monolayer due to increasing van der Waals interactions. For didecanoyl PA, the singly deprotonated species is dominant between pH 4 and 5.6 (Figure 3) as observed through the lowering of the apparent MMA. The change in protonation state for didecanoyl PA between pH 4 to 5.6 is evident from transition between the surface active fully-protonated monolayer to the less surface active negatively charged species that desorbs into bulk solution as pH increases.

2.2 IRRAS spectra reveals a depleting monolayer at higher pH

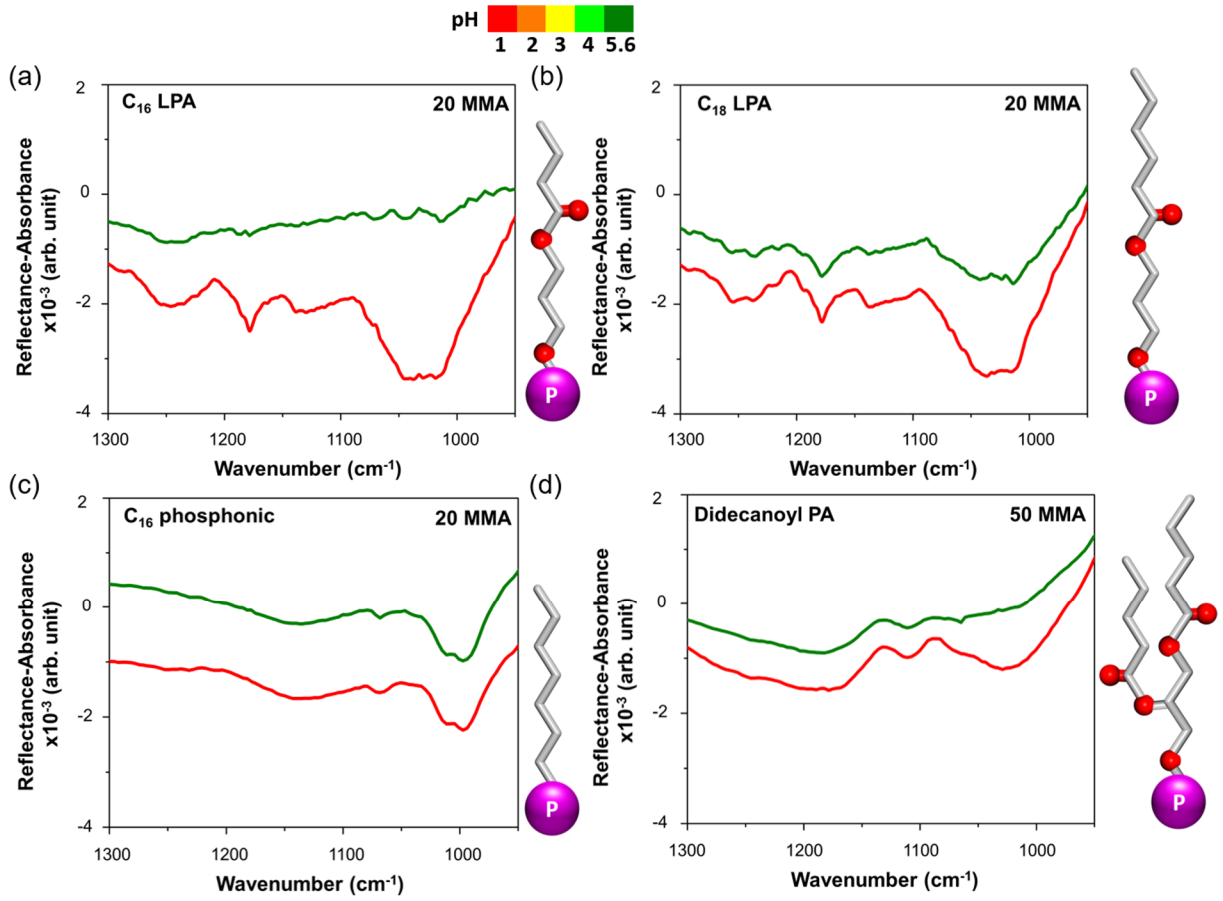

Figure S2. IRRAS spectra of (a) C_{16} LPA, (b) C_{18} LPA on pH 1 and pH 5.6 at 20 MMA and (c) C_{16} phosphonic acid and (d) didecanoyl PA on pH 1 and pH 5.6 at 20 MMA. The disappearance of the phosphate peaks for the LPAs at higher pH suggests desorption of the molecules.

2.3 Brewster Angle Microscopy reveals changing molecular interactions

BAM images of the semi-soluble species were taken at bulk pH values of 1, 2, 3, 4, and 5.6 (Figure S3, columns 1-5). BAM images at constant apparent MMA were chosen for each molecule across the pH range 1 to 5.6. It is evident that as pH decreases, the C_{16} LPA domains become brighter (Figure S3, row 1, from right to left) due to an increase in surface activity, which

agrees with the trend observed in the Π-A isotherms. Small circular domains were observed for C_{16} LPA at pH 1 (Figure S3, row 1), whereas C_{18} LPA has much more closely packed domains (Figure S3, row 2). Comparing the C_{16} LPA to the C_{18} LPA, the C_{18} LPA displays more surface activity at higher pH shown by the presence of small islands at pH 5.6 (Figure S4, row 5) and substantial coverage at pH 4 (Figure S5, row 4), while the C_{16} LPA images are much darker at higher pH (Figure S5, rows 3-5).

Overall, BAM results for the C_{16} and C_{18} LPAs are consistent with the Π-A isotherms, revealing that the strength of van der Waals interactions leads to changes in stability, and the overall propensity to form monolayers at high pH for these semi-soluble species. In comparison to the LPAs, the single chain C_{16} phosphonic acid (Figure S3, row 3) and the double chain didecanoyl PA (Figure S3, row 4) do not show much variation in the BAM images between pH 1 to 5.6. Across a fixed apparent MMA, the C_{16} phosphonic acid images are observed in the condensed phase regardless of pH, thus the molecular density does not change significantly. For the didecanoyl PA, the images are uniformly dark, as expected since the molecules do not pack tightly as evidenced by the large MMA in the liftoff point (Figure S3, bottom row).

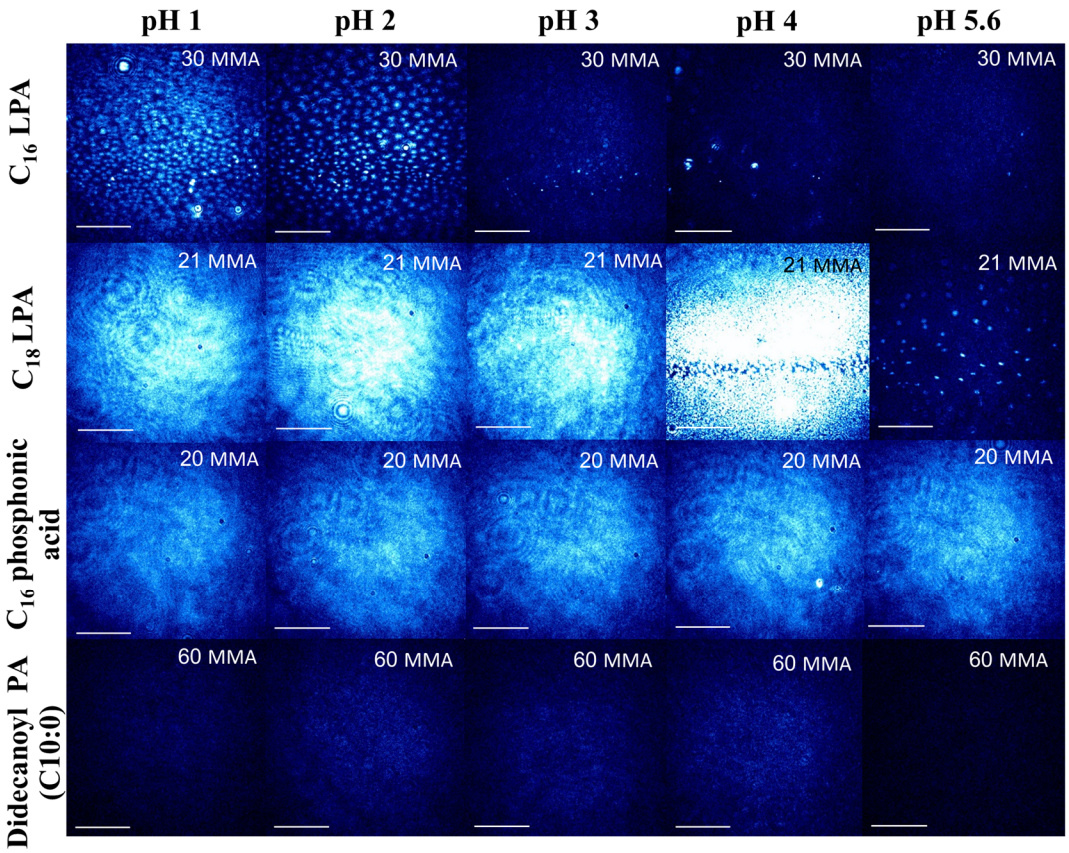

Figure S3. BAM images of C_{16} LPA at 30 MMA, C_{18} LPA at 21 MMA, C_{16} phosphonic acid at 20 MMA, didecanoyl PA at 60 MMA (top to bottom) on pH 1, 2, 3, 4, and 5.6 (left to right). Scale bars shown are 50 μm.

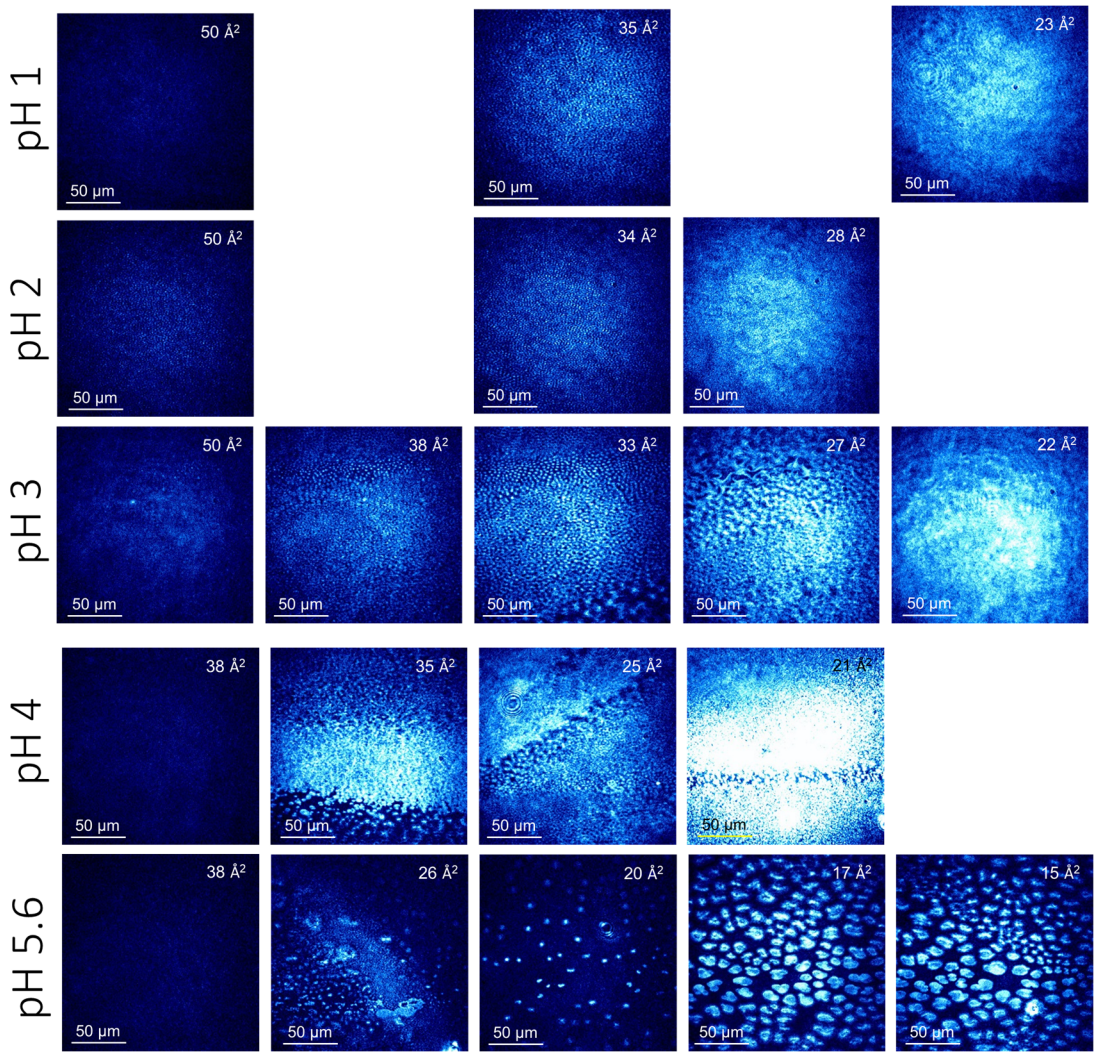

Figure S4. BAM images of C_{18} LPA taken at multiple MMAs at pH 1 to 5.6 to show the changes in morphology during the isotherm compression at different pH.

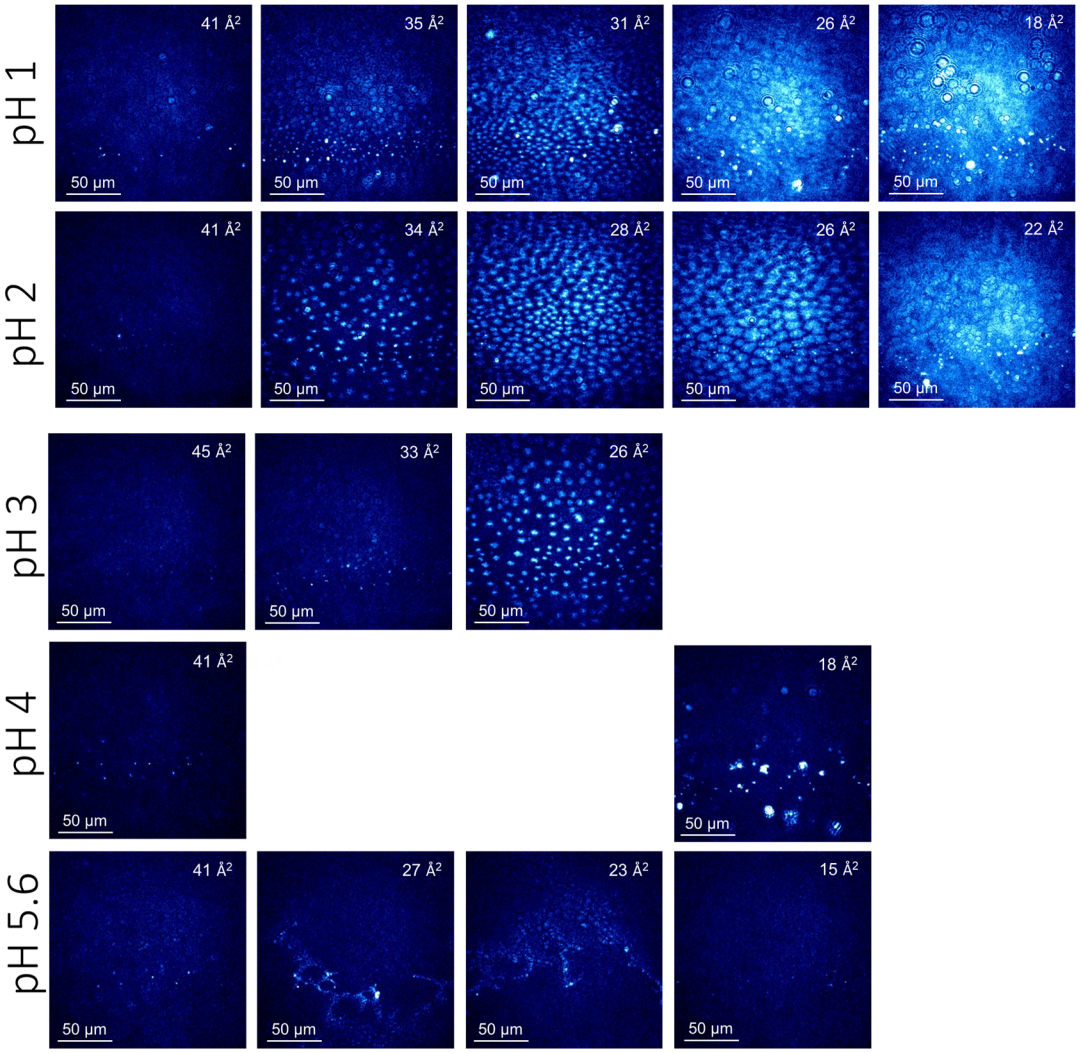

Figure S5. BAM images of C_{16} LPA taken at multiple MMAs at pH 1 to 5.6 to show the changes in morphology during the isotherm compression at different pH.

2.4 Vibrational assignments for the phosphonic acid species

Geometry optimization and harmonic vibrational frequency calculations of fully protonated (Figure S6a) and singly deprotonated (Figure S6b) truncated hexadecylphosphonic acid (C_{16} phosphonic acid) were conducted using Q-Chem v. 5.2.[11] Density functional theory (DFT) at the B3LYP/6-31G* level of theory[12] and a conductor polarizable continuum model (CPCM)[13,14] with a dielectric constant of 78.39 were used, and a vibrational frequency scaling factor of 0.9614

was applied.[15] Vibrational frequencies, intensities, and mode assignments within the frequency region of the phosphonic acid headgroup vibrational modes (900-1220 cm^{-1}) are tabulated in Tables S1 and S2.

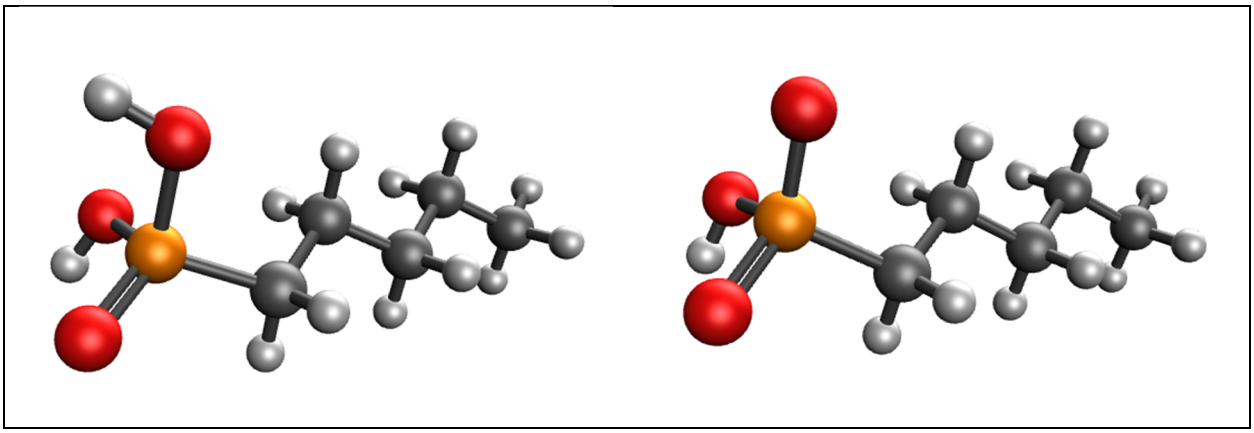

Figure S6. Optimized structures of (a) fully protonated and (b) singly deprotonated truncated hexadecylphosphonic acid (C_{16} phosphonic acid).

Table S1. Harmonic vibrational frequencies, intensities, and vibrational mode assignments of the truncated fully protonated (H_2PO_3) C_{16} phosphonic acid.

Wavenumber (cm^{-1})	**Intensity (km/mol)**	**Mode Assignment**
923.30	17.763	CH_2 twisting + CH_2 rocking + POH symmetric bending
971.37	3.409	C-C stretching + POH symmetric bending + CH_3 wagging
999.90	39.318	POH symmetric bending + C-C stretching + CH_2 twisting
1009.43	50.194	POH symmetric bending + C-C stretching + CH_2 twisting
1023.26	139.791	Asymmetric POH bending

1026.73	1.841	C-C stretching + asymmetric POH bending
1054.58	40.918	Symmetric POH bending + CH_2 twisting
1086.05	8.534	CH_2 + CH_3 wagging
1175.13	256.416	P=O stretching + POH bending, CH_2 wagging
1184.86	2.433	CH_2 twisting + rocking
1190.55	47.042	CH_2 wagging
1216.76	121.757	CH_2 wagging + P=O stretching + symmetric POH bending

Table S2. Harmonic vibrational frequencies, intensities, and vibrational mode assignments of the truncated singly deprotonated (HPO_3^-) C_{16} phosphonic acid.

Wavenumber (cm^{-1})	**Intensity (km/mol)**	**Mode Assignment**
913.80	11.001	CH_2 twisting + CH_2 rocking + POH bending
970.63	4.095	POH bending + C-C stretching + CH_3 wagging
988.89	179.441	POH bending + CH_2 twisting
1008.06	0.709	POH bending + C-C stretching
1011.93	146.229	O=P-O^- symmetric stretching + CH_2 twisting
1024.71	0.992	C-C-C asymmetric stretching
1036.88	90.616	POH bending + O=P-OH asymmetric stretching + CH_2 twisting
1082.21	10.560	CH_2 + CH_3 wagging
1178.38	160.588	O=P-O^- asymmetric stretching + POH bending + CH_2 twisting + CH_2 rocking
1185.81	116.986	O=P-O^- asymmetric stretching + POH bending + CH_2 twisting
1197.92	151.484	O=P-O^- asymmetric stretching + POH bending + CH_2 wagging

3. GOUY-CHAPMAN DEPROTONATION CALCULATION AND DISCUSSION

The form of the Gouy-Chapman model used in this manuscript is derived from the Boltzmann equation

$$K_a = \frac{[A^-]_0[H^+]_0}{[HA]_0} = \frac{\alpha}{1-\alpha}[H^+]_0 = \frac{\alpha}{1-\alpha}[H^+]_\infty e^{-e\Psi_0/kT}$$

where K_a is the equilibrium constant, a is the degree of deprotonation, e is the fundamental charge, Ψ_0 is the surface potential, k is the Boltzmann constant, and T is the temperature. The Boltzmann equation relates the surface proton concentration $[H^+]_0$ to the bulk proton concentration $[H^+]_\infty$.[16] Plotting the form of the Boltzmann equation as a function of temperature reveals that the surface proton concentration increases with temperature, although the magnitude of the change is small (Figure S7).

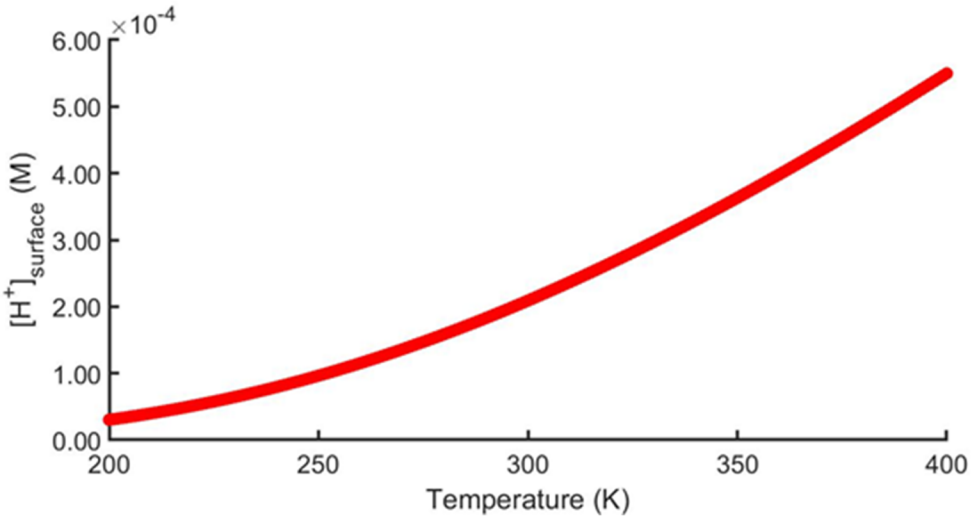

Figure S7. Surface proton concentration as a function of temperature using a surface potential value of Ψ_0 = -100 mV, a value relevant for soluble surfactants.[17]

Other models have been developed since Gouy and Chapman applied their theory of the electrostatic double layer to planar surfaces with varying degrees of success. Increasing physical relevance is generally accompanied by increasing model complexity, sometimes with only marginal increases in accuracy. A detailed discussion of adsorption models can be found in Peng and Nguyen, 2020.[18] We will briefly summarize the four main classes of adsorption models.

Davies et al.[19] developed a model to describe an infinitely-thin charged layer that attracts oppositely-charged counterions to form a diffuse layer, but its quantitative agreement with experimental results is poor.[20] Borwankar and Wasan[21] (BW) expanded upon the Davies model to include a parameter for intermolecular interactions, and the BW model generally agrees well with experiment. The Gouy-Chapman, Davies, and BW models use the Grahame equation to relate adsorbed ion species and interfacial potential; and all three are inherently limited by the validity of the Grahame equation.[22]

To counteract the high interfacial potentials induced by large ion concentrations in the adsorption layers predicted by the Davies and BW models, counterion binding models were developed. Specifically, Kralchevsky et al.[23] applied the Stern adsorption isotherm to model the relationship between adsorbed surfactant headgroups and binding counterions. Kalinin and Radke[24] (KR model) developed a more complex model to describe discrete surfactant and counterion adsorption layers, and the diffuse counterion layer assumes Gouy-Chapman behavior.

The counterion binding models assume a single surfactant monolayer, so surfactant immersion models were developed to account for thick interfacial surfactant adsorption layers. The Shahir model[25] again uses the Grahame equation to describe the relationship between the surfactant adsorption layers and the diffuse counterion layer. While this model more accurately describes ionic distribution across the air-water interface, the surfactant immersion depth

parameter can only be definitively determined with additional MD simulations, neutron reflection experiments, or neutral impact collision ion scattering spectroscopy (NICISS) experiments. Otherwise, the fitted surfactant immersion depth parameter is inextricably related to the fitted intermolecular interaction parameter.[25]

Modified Poisson-Boltzmann equation-based models improve upon the assumptions of the Grahame equation by accounting for image charges and dispersion forces in addition to electrostatic forces.[17,26–28] These models generally produce the best agreement with experiment. However, MD simulations are needed to fully parameterize these models.

4. REFERENCES

(1) Hua, W.; Verreault, D.; Adams, E. M.; Huang, Z.; Allen, H. C. Impact of Salt Purity on Interfacial Water Organization Revealed by Conventional and Heterodyne-Detected Vibrational Sum Frequency Generation Spectroscopy. *Journal of Physical Chemistry C* **2013**, *117* (38), 19577–19585.

(2) Zhang, T.; Cathcart, M. G.; Vidalis, A. S.; Allen, H. C. Cation Effects on Phosphatidic Acid Monolayers at Various pH Conditions. *Chemistry and Physics of Lipids* **2016**, *200*, 24–31.

(3) Adams, E. M.; Allen, H. C. Palmitic Acid on Salt Subphases and in Mixed Monolayers of Cerebrosides: Application to Atmospheric Aerosol Chemistry. *Atmosphere* **2013**, *4*, 315–336.

(4) Gershfeld, N. L.; Pak, C. Y. O. The Surface Chemistry of Monooctadecyl Phosphate at the Air/Water Interface. A Study of Molecular Aggregation in Monolayers. *Journal of Colloid and Interface Science* **1967**, *23* (2), 215–220.

(5) Gaines, G. L. *Insoluble Monolayers at Liquid-Gas Interfaces*; Interscience Publishers: New York, 1966.

(6) Spink, J. A. Ionization of Monolayers of Fatty Acids from C_{14} to C_{18}. *Journal of Colloid Science* **1963**, *18* (6), 512–525.

(7) Ries, H. E.; Cook, H. D. Monomolecular Films of Mixtures: I. Stearic Acid with Isostearic Acid and with Tri-*p*-Cresyl Phosphate. Comparison of Components with Octadecylphosphonic Acid and with Tri-*o*-Xenyl Phosphate. *Journal of Colloid Science* **1954**, *9* (6), 535–546.

(8) Woodward, J. T.; Ulman, A.; Schwartz, D. K. Self-Assembled Monolayer Growth of Octadecylphosphonic Acid on Mica. *Langmuir* **1996**, *12* (15), 3626–3629.

(9) He, W.; Jiang, C.; Liu, F.; Tai, Z.; Liang, Y.; Guo, Z.; Zhu, L. Monolayer Formation of Alkyl Chain-Containing Phosphoric Acid Amphiphiles at the Air/Water (pH 5.6) Interface: Influence of Temperature and Cations. *Journal of Colloid and Interface Science* **2002**, *246* (2), 335–342.

(10) Perrin, D. D. *Ionisation Constants of Inorganic Acids and Bases in Aqueous Solution*; Pergamon Press: New York, 1982.

(11) Shao, Y.; Gan, Z.; Epifanovsky, E.; Gilbert, A. T. B.; Wormit, M.; Kussmann, J.; Lange, A. W.; Behn, A.; Deng, J.; Feng, X.; Ghosh, D.; Goldey, M.; Horn, P. R.; Jacobson, L. D.; Kaliman, I.; Khaliullin, R. Z.; Kuś, T.; Landau, A.; Liu, J.; Proynov, E. I.; Rhee, Y. M.; Richard, R. M.; Rohrdanz, M. A.; Steele, R. P.; Sundstrom, E. J.; Woodcock, H. L.; Zimmerman, P. M.; Zuev, D.; Albrecht, B.; Alguire, E.; Austin, B.; Beran, G. J. O.; Bernard, Y. A.; Berquist, E.; Brandhorst, K.; Bravaya, K. B.; Brown, S. T.; Casanova, D.; Chang, C.-M.; Chen, Y.; Chien, S. H.; Closser, K. D.; Crittenden, D. L.; Diedenhofen, M.; DiStasio, R. A.; Do, H.; Dutoi, A. D.; Edgar, R. G.; Fatehi, S.; Fusti-Molnar, L.; Ghysels, A.; Golubeva-Zadorozhnaya, A.; Gomes, J.; Hanson-Heine, M. W. D.; Harbach, P. H. P.; Hauser, A. W.; Hohenstein, E. G.; Holden, Z. C.; Jagau, T.-C.; Ji, H.; Kaduk, B.; Khistyaev, K.; Kim, J.; Kim, J.; King, R. A.; Klunzinger, P.; Kosenkov, D.; Kowalczyk, T.; Krauter, C. M.; Lao, K. U.; Laurent, A. D.; Lawler, K. V; Levchenko, S. V; Lin, C. Y.; Liu, F.; Livshits, E.; Lochan, R. C.; Luenser, A.; Manohar, P.; Manzer, S. F.; Mao, S.-P.; Mardirossian, N.; Marenich, A. V; Maurer, S. A.; Mayhall, N. J.; Neuscamman, E.; Oana, C. M.; Olivares-Amaya, R.; O'Neill, D. P.; Parkhill, J. A.; Perrine, T. M.; Peverati, R.; Prociuk, A.; Rehn, D. R.; Rosta, E.; Russ, N. J.; Sharada, S. M.; Sharma, S.; Small, D. W.;

Sodt, A.; Stein, T.; Stück, D.; Su, Y.-C.; Thom, A. J. W.; Tsuchimochi, T.; Vanovschi, V.; Vogt, L.; Vydrov, O.; Wang, T.; Watson, M. A.; Wenzel, J.; White, A.; Williams, C. F.; Yang, J.; Yeganeh, S.; Yost, S. R.; You, Z.-Q.; Zhang, I. Y.; Zhang, X.; Zhao, Y.; Brooks, B. R.; Chan, G. K. L.; Chipman, D. M.; Cramer, C. J.; Goddard, W. A.; Gordon, M. S.; Hehre, W. J.; Klamt, A.; Schaefer, H. F.; Schmidt, M. W.; Sherrill, C. D.; Truhlar, D. G.; Warshel, A.; Xu, X.; Aspuru-Guzik, A.; Baer, R.; Bell, A. T.; Besley, N. A.; Chai, J.-D.; Dreuw, A.; Dunietz, B. D.; Furlani, T. R.; Gwaltney, S. R.; Hsu, C.-P.; Jung, Y.; Kong, J.; Lambrecht, D. S.; Liang, W.; Ochsenfeld, C.; Rassolov, V. A.; Slipchenko, L. V; Subotnik, J. E.; Van Voorhis, T.; Herbert, J. M.; Krylov, A. I.; Gill, P. M. W.; Head-Gordon, M. Advances in Molecular Quantum Chemistry Contained in the Q-Chem 4 Program Package. *Molecular Physics* **2015**, *113* (2), 184–215.

(12) Becke, A. D. Density-Functional Thermochemistry. III. The Role of Exact Exchange. *Journal of Chemical Physics* **1993**, *98* (7), 5648-5652.

(13) Barone, V.; Cossi, M. Quantum Calculation of Molecular Energies and Energy Gradients in Solution by a Conductor Solvent Model. *The Journal of Physical Chemistry A* **1998**, *102* (11), 1995–2001.

(14) Takano, Y.; Houk, K. N. Benchmarking the Conductor-like Polarizable Continuum Model (CPCM) for Aqueous Solvation Free Energies of Neutral and Ionic Organic Molecules. *Journal of Chemical Theory and Computation* **2005**, *1* (1), 70–77.

(15) Scott, A. P.; Radom, L. Harmonic Vibrational Frequencies: An Evaluation of Hartree−Fock, Møller−Plesset, Quadratic Configuration Interaction, Density Functional Theory, and Semiempirical Scale Factors. *The Journal of Physical Chemistry* **1996**, *100* (41), 16502–16513.

(16) Tyrode, E.; Corkery, R. Charging of Carboxylic Acid Monolayers with Monovalent Ions at Low Ionic Strengths: Molecular Insight Revealed by Vibrational Sum Frequency Spectroscopy. *J. Phys. Chem. C* **2018**, *122* (50), 28775–28786.

(17) Peng, M.; Duignan, T. T.; Zhao, X. S.; Nguyen, A. V. Surface Potential Explained: A Surfactant Adsorption Model Incorporating Realistic Layer Thickness. *J. Phys. Chem. B* **2020**, *124* (15), 3195–3205.

(18) Peng, M.; Nguyen, A. V. Adsorption of Ionic Surfactants at the Air-Water Interface: The Gap between Theory and Experiment. *Advances in Colloid and Interface Science* **2020**, *275*, 102052.

(19) Davies, J. T.; Rideal, E. K. Adsorption of Long-Chain Ions. I. *Proceedings of the Royal Society of London. Series A. Mathematical and Physical Sciences* **1958**, *245* (1242), 417–428.

(20) Lucassen-Reynders, E. H. Surface Equation of State for Ionized Surfactants. *J. Phys. Chem.* **1966**, *70* (6), 1777–1785.

(21) Borwankar, R. P.; Wasan, D. T. Equilibrium and Dynamics of Adsorption of Surfactants at Fluid-Fluid Interfaces. *Chemical Engineering Science* **1988**, *43* (6), 1323–1337.

(22) Newman, J.; Thomas-Alyea, K. E. *Electrochemical Systems*; John Wiley & Sons, 2012.

(23) Kralchevsky, P. A.; Danov, K. D.; Broze, G.; Mehreteab, A. Thermodynamics of Ionic Surfactant Adsorption with Account for the Counterion Binding: Effect of Salts of Various Valency. *Langmuir* **1999**, *15* (7), 2351–2365.

(24) Kalinin, V. V.; Radke, C. J. An Ion-Binding Model for Ionic Surfactant Adsorption at Aqueous-Fluid Interfaces. *Colloids and Surfaces A: Physicochemical and Engineering Aspects* **1996**, *114*, 337–350.

(25) Shahir, A. A.; Nguyen, A. V.; Karakashev, S. I. A Quantification of Immersion of the Adsorbed Ionic Surfactants at Liquid|fluid Interfaces. *Colloids and Surfaces A: Physicochemical and Engineering Aspects* **2016**, *509*, 279–292.
(26) dos Santos, A. P.; Levin, Y. Surface Tensions and Surface Potentials of Acid Solutions. *J. Chem. Phys.* **2010**, *133* (15), 154107.
(27) Duignan, T. T.; Peng, M.; Nguyen, A. V.; Zhao, X. S.; Baer, M. D.; Mundy, C. J. Detecting the Undetectable: The Role of Trace Surfactant in the Jones-Ray Effect. *J. Chem. Phys.* **2018**, *149* (19), 194702.
(28) Uematsu, Y.; Bonthuis, D. J.; Netz, R. R. Charged Surface-Active Impurities at Nanomolar Concentration Induce Jones–Ray Effect. *J. Phys. Chem. Lett.* **2018**, *9* (1), 189–193.